ADVANCED INTELLIGENT SYSTEMS
Open Access
www.advintellsyst.com

RESEARCH ARTICLE OPEN ACCESS

Cooptimized Sensing and Sole Mechanics Enable Embodied-Intelligence Design of User-Specific Smart Footwear

Fengyu Zhong | Marco Pontin | Amy Zavatsky | Perla Maiolino

Engineering Science Department, University of Oxford, Oxford, UK

Correspondence: Perla Maiolino (perla.maiolino@eng.ox.ac.uk)

Received: 7 February 2026 | **Revised:** 19 May 2026 | **Accepted:** 25 May 2026

Keywords: embodied cognition | gait (human) | lattice materials | soft sensing | wearable systems

ABSTRACT

Research in embodied intelligence has proven that the embodiment of a system, its physical structure and morphology, shapes how it senses and processes information. Here, we introduce an embodied codesign framework for user-centric wearables and apply it to the design of smart footwear. The pipeline jointly optimizes mechanical and sensing properties of the 3D printed lattice sole for efficient and effective plantar pressure monitoring. The result is a customized wearable device with tuned regional properties and minimal onboard sensing capable of real-time centre-of-pressure tracking in line with commercial pressure plate devices while reducing sensor count and energy demand. Furthermore, our embodied codesign improves sensitivity by 52% with respect to uniform stiffness state-of-the-art design approaches, demonstrating how cooptimizing structure and sensing can transform wearables into morphologically intelligent systems, paving the way toward predictive, energy-efficient, and personalized health monitoring.

1 | Introduction

Progress in technology and AI is making itpossible for medicine to shift from disease prevention and treatment to disease prediction through continuous monitoring and processing of key biomarkers [1, 2]. Realizing this vision, though, requires personalized wearable devices that collect just enough high-quality data for accurate prediction while minimizing energy and computation demands for on-device edge-computing. Achieving this balance remains a central challenge in wearable sensor design. A promising path is “embodied codesign,” where the structure of a device is optimized alongside its sensing capabilities to directly shape the kind of data it generates. In this paradigm, mechanical morphology is not a passive support for sensors but an active element that filters, amplifies, and structures sensory information.

Inspired by how biological organisms exploit their embodiment to filter and process sensory information before neural computation occurs, research in embodied intelligence highlights that the physical form of a system, its geometry, stiffness, and material dynamics, can actively shape how information is sensed and processed to simplify the control problem [3–6]. In this paradigm, compute, sensing and mechanics are not treated as separate and modular but jointly optimized, yielding advances in soft robotics and morphologically adaptive materials [7–10]. Yet, their systematic application to wearable sensors remains largely unexplored. Codesigning the mechanical structure and sensing architecture of wearables offers an avenue toward devices that compute through morphology, improving data quality and efficiency at the hardware level whilst allowing the structure to satisfy key mechanical performance requirements.

Fengyu Zhong and Marco Pontin contributed equally to the study.

Smart footwear provides a particularly interesting testbed for embodied codesign, as devices must be power-efficient, low-cost, highly-customizable, and capable of tracking plantar pressure in real time and at high throughput for accurate centre of pressure (CoP) estimation during fast gait events [11–17]. However, much of the current research follows a sensor-centric design paradigm, focusing on novel sensor technologies and fabrication techniques [11, 14, 18–23], rather than on codesigns tailored to a specific user's mechanical and sensing requirements. As many sensors as possible are integrated, favoring spatial resolution, even though studies indicate how optimized placement of few sensors in key plantar locations allows for good reconstruction [15–17] with minimal user data [24]. In addition, devices exhibit homogeneous stiffness [11, 13, 14] with sensing ranges largely below peak pressures normally observed in real world [25] and the shoe stiffness and its interaction with the insole devices are usually neglected [13, 14, 26]. The cooptimisation of lattice structural properties with sensing requirements such as sensor range, spatial resolution, number, and placement informed by user-specific data remains largely unexplored. More broadly, this highlights a missed opportunity to use mechanical structure itself as part of the sensing strategy.

A small amount of precollected user data together with the desired sensor performance characteristics are used to select the optimal lattice structure for the smart sole to provide appropriate plantar support and high-quality sensor output. Pneumatic chambers coupled to the lattice voids in key optimal locations allow for direct plantar pressure measurements while also minimizing overall sensor number, which allows for fast wireless readout speeds and efficient operation of the device.

In the quest toward embodied intelligence design of smart wearables, lattice-based structures and metamaterials provide great potential, as mechanical properties such as stiffness and weight can be easily tuned by adjusting the unit cell geometry [27, 28]. The lattices themselves can also become sensing elements via piezoresistive [29] or capacitive effects [30]. Pneumatic sensing in particular offers an alternative less susceptible to electromagnetic interference [31] that does not rely on functionalized materials. Furthermore, lattice structures inherently provide cavities that can be adapted to house air chambers for direct pressure measurement, whilst additive manufacturing allows highly customizable geometries [32–34].

We present a design and manufacturing pipeline, displayed in Figure 1, for user-centric 3D printed lattice-based smart soles in which user plantar pressure data guide the cooptimization of lattice geometry and sensing parameters. This embodied codesign treats the sole's morphology as an active component of the sensing pipeline. This embodied codesign enables regional tuning of stiffness, sensing range, and spatial resolution within a single monolithic structure, allowing sensing performance to be shaped at the hardware level rather than through postprocessing alone. Integrated pneumatic chambers and embedded electronics support wireless data logging and real-time CoP tracking. We validate the system against commercial pressure plates and demonstrate its operation in everyday activities. Although demonstrated here in smart footwear, the proposed framework is applicable to a broad class of wearable and soft sensing systems, including orthotics, prosthetics, rehabilitation devices, and robotic skins, wherever mechanical compliance and sensing efficiency must be jointly optimized.

2 | Methods

2.1 | The Smart Shoe Device Design

The smart shoe consists of three layers (Figure S1): a 3D printed lattice-structure sole; a unit encasing the sensing electronics

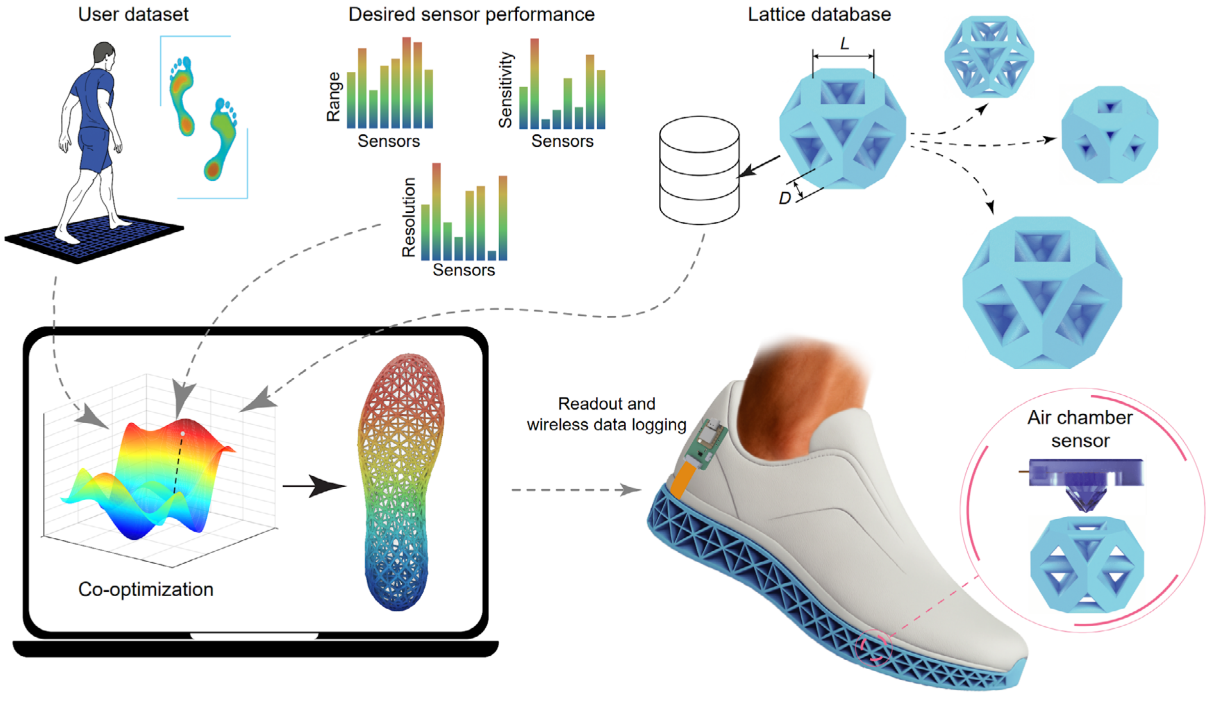

FIGURE 1 | The embodied intelligence-inspired cooptimization pipeline.

housed in airtight pyramidal pneumatic chambers; a shoe upper holding readout electronics and a battery. The pyramidal chambers are shaped to fit inside the lattice cavities in key locations across the sole.

As the user steps on the sole, the deformation in the lattice structure causes pressure changes in the air chambers, which are measured by the sensing electronics. These measurements are then converted back to foot pressure data used for CoP tracking in real time.

2.2 | Optimized Sensor Placement

The placement of eight sensor units was determined using the method described in [24] (Supplementary Materials and Methods and Figure 2). High-resolution plantar pressure data were first processed by vectorizing each frame of the pressure map and concatenating all frames horizontally. Principal component analysis was then applied to the concatenated array. The first principal component, which explained over 50% of the total variance, and its corresponding loading coefficient matrix (LCM)—

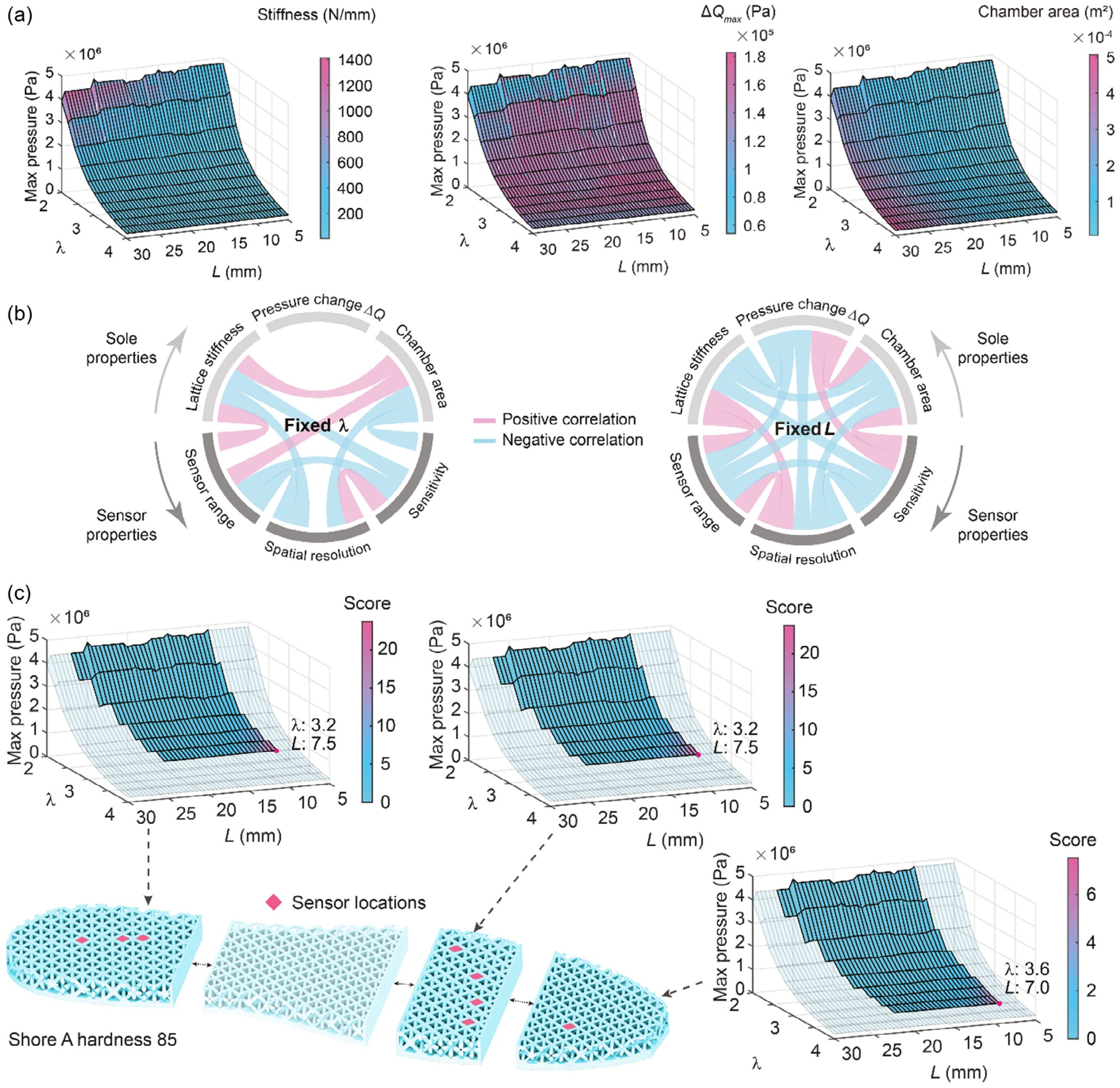

FIGURE 2 | Lattice database and optimization results. (a) Relationship between the defining lattice parameters λ and L and key sole properties – equivalent stiffness K, predicted maximum air pressure change inside the chamber $\Delta Q_{\max}$ and chamber area A_c. (b) Qualitative analysis of the correlation between sole properties and final sensor characteristics. Some relationships can be inferred from the gradients of the charts in subfigure a, while others are derived directly from the lattice geometry. (c) Having defined a scoring function and user-tailored constraints, optimal lattices are selected for the 3 different parts of the sole integrating pressure sensors. For each region, the highest scoring lattice was selected each time and sensors were integrated in the optimal locations.

with absolute values taken—were extracted. Inspection of the LCM revealed that the subject exhibited no noticeable midfoot loading, suggesting a neutral to high arch in the foot; hence, no sensors were placed there. For the heel region, a loading coefficient threshold was selected such that 90% of the LCM volume was contained below it. The heel region was then approximated as an ellipsoid, and its long axis was identified. A ridge line was generated by scanning for local peaks along this long axis, and three sensors were positioned at the centre and the two ends of this ridge. For the forefoot region, four sensors were evenly distributed across the region based on visual inspection of the LCM. Finally, a single prominent peak corresponding to the big toe was detected in the LCM, where one sensor was placed.

The placement method was also compared against a spread-out benchmark placement strategy inspired by [35] demonstrating substantially superior CoP tracking performance (Supplementary Materials and Methods, Figure S2).

2.3 | Device Fabrication and Integration

The sole was fabricated using PolyJet 3D printing on a Stratasys J735, with Agilus 30 and Vero materials digitally mixed to achieve the different hardnesses required for each part of the device. A soluble support material, SUP706B was used to simplify postprocessing. For the latticed sole, a material with Shore A hardness 85A was selected based on preliminary results [36], as it is the softest option capable of withstanding the maximum plantar pressure in the population dataset [25]. Selecting the softest viable material maximized the range of achievable lattice mechanical and sensing properties. A Shore A hardness of 30A was selected for the other compliant components. The shoe upper was adapted from a commercial sneaker.

The PCB–sensor module comprises a flexible PCB carrying barometric sensors (STMicroelectronics ILPS22QS), integrated during printing within a compliant Agilus 30 casing that integrates the pneumatic air chambers. To ensure airtightness of the chambers, a process combining the use of cyanoacrylate glue was devised as shown in Figure S6.

2.4 | Lattice Design and FEA Analyses

The octet-truss lattice was selected due to its superior mechanical performance reported in the literature, including high stiffness, strength, strength-to-weight ratio, near-isotropic behavior, and favorable energy absorption characteristics [37–40]. In addition, its open-cell geometry facilitates the integration of air chambers. The unit cell is characterized by the strut length L and diameter D.

The ratio $\lambda = \frac{L}{D}$ is representative of the relative volumetric density of the lattice, with a smaller λ representing a higher density. The chamber area A_c is defined as

$$A_c = (L - D)^2 \tag{1}$$

To characterize the mechanical properties of a wide range of lattice configurations, finite element modeling (FEM) simulations were conducted with Ansys 2020 R1 and set up as shown in Figure S7, with an indenter pressing on a reference unit cell.

Based on the plantar pressure dataset from [25], simulations were conducted on lattice configurations with strut length $L = \{5, 10, 12.5, 15, 17.5, 20, 25, \text{and } 30\}$ mm and density ratio $\lambda \in [2.0, 4.0]$ ($\lambda \geq 2$ for support removal and housing of the electronic sensors) with step of 0.2. These correspond to lattice layer heights of 7.07–42.4 mm, consistent with typical shoe sole thicknesses. The FEM results were then linearly interpolated for intermediate L values at 0.5 mm increments for each fixed λ. The simulations utilized a first-order Yeoh material model for Shore 85A derived from material characterization (Supplementary Materials and Methods), while the indenter was modeled as structural steel to ensure stiffness that far exceeds that of the lattice.

The maximum pressure $P_{\max}$ the lattice can withstand is defined as the highest applied pressure at which the FEM simulation is still able to converge. The equivalent stiffness K of each unit cell is then derived as

$$K = \frac{P_{\max} A}{\Delta H_{\max}} \tag{2}$$

where A is the indenter area and $\Delta H_{\max}$ is the maximum compression depth at FEM convergence.

2.5 | Air Chamber Modeling

The air chamber is pyramid-shaped to fit within the lattice cavity, with a 1 mm wall thickness determined experimentally to balance minimal thickness and structural robustness. The design leaves the lattice struts uninterrupted, preserving the lattice's mechanical behavior.

An analytical model was developed to predict the chamber air pressure change directly from the lattice FEM results, under the assumption that air chambers—made of material (Shore 30A) that is much softer than that of the lattice (Shore 85A)—add a negligible amount of stiffness to the lattice. Assuming the compression of the air chamber is adiabatic, the pressure change ΔQ within it is given by

$$\Delta Q = Q_0 \left(\frac{V_0}{V} \right)^{\gamma} - Q_0 \tag{3}$$

where Q_0 is the initial chamber pressure, V_0 and V are the chamber volumes before and after compression respectively, and $\gamma = 1.4$ is the adiabatic index of air. Further approximating the chamber as a pyramid with fixed base area and variable height, the volume ratio reduces to the height ratio. The pressure change can thus be expressed as

$$\Delta Q = Q_0 \left(\frac{H_0}{H_0 - \Delta H} \right)^{\gamma} - Q_0 \tag{4}$$

where H_0 and ΔH represent the initial chamber height and its change. The maximum chamber air pressure change $\Delta Q_{\max}$ can therefore be estimated at $\Delta H_{\max}$.

To validate the assumption that the chamber walls contribute negligibly to stiffness, two FEM models of a single lattice unit cell were compared: one including the chamber walls and one without (Figure S8). Simulations were conducted on a unit cell with the lowest stiffness K ($\lambda = 4.0$, $L = 5$ mm). Under an applied pressure $P_{\max}$ of 84 kPa (a pressure far below typical human peak plantar pressure), the model with chamber walls showed a stiffness of $2470\,\mathrm{Nm}^{-1}$ compared to $2084\,\mathrm{Nm}^{-1}$ without walls, an increase of only 18.5%. This effect further diminishes as lattice stiffness increases or as multiple lattice layers are stacked.

The analytical model was validated by applying it to the sensor calibration dataset to estimate the compression pressure which was then compared with the ground truth provided by the load cell (details in the next section). To such end. The previous equation was modified to get the estimated compression pressure P_{est} as a function of ΔQ and lattice stiffness K

$$P_{\mathrm{est}} = K_{\exp}\left(H_0 + \frac{3B}{A_c}\right)\left[1 - \left(\frac{Q_0}{Q}\right)^{\frac{1}{\gamma}}\right]\left(\frac{1}{A_c}\right) \tag{5}$$

where B represents the dead volume within the air chambers and $K_{\exp}$ is the lattice stiffness measured during the experiment.

The predictions for each sensor were then compared against the corresponding measured compression pressures P, as shown in Figure S4. The full-scale normalized root mean square error averaged 14.0% with a standard deviation of 3.26% across all sensors, indicating low error and validating the analytical model.

2.6 | Device Calibration

Sensor calibration was performed using a 3-axis Cartesian robot (Figure S9). The setup included a load cell with a data logger and indenters, 3D prited in PolyLactic Acid (PLA) on a Carbon X printer (Bambu Lab, China), shaped to match the dimensions of each regional lattice. The robot applied cyclic, displacement-controlled compressions at pressures exceeding the required P_{reg} for each of the eight sensor locations.

During calibration, compression force from the load cell and internal air pressure from the device were recorded simultaneously. The final three compression cycles, where the response had stabilized, were extracted for analysis. The signals were postprocessed to obtain the compression pressure P and air pressure change ΔQ, defined as the change relative to the sensor's initial reading at power-up. An average R^2 of 0.937 between P and ΔQ was observed across all sensor locations. A power-law relationship with an offset was observed between all pairs of ΔQ and P. Accordingly, power-law regression models were fitted

$$P = a(\Delta Q)^b + c \tag{6}$$

The offset term c accounts for residual chamber pressure caused by slow and incomplete lattice recovery between compression cycles. The fitted models achieved an average R^2 of 0.955 with a standard deviation of 0.0106 across all eight sensors (Figure S4).

2.7 | Controlled Gait Experiments

Gait experiments were conducted using a treadmill to provide controlled and repeatable test conditions. The experiments were intended to provide functional validation of plantar pressure sensing and CoP tracking performance. Walking speeds were set to 4 and 5 km/h for slow and fast walking, respectively. The treadmill's maximum inclination of 8.5° was used for the inclined conditions. Four scenarios were tested: fast flat walking, slow flat walking, fast inclined and slow inclined walking. Data for all scenarios were collected in a single session, with 15 steps recorded per scenario (Video S1). A short transition period was included between scenarios to allow the treadmill to reach the target speed and inclination. The regression fitting (Figure S4) was then used to map the air pressure change to plantar pressure. The data was postprocessed to segment it into trials, each containing a single stance phase. During the process, the delayed return to baseline in the sensor signals caused by the viscoelastic material was also compensated. The start of a stance phase was defined as the instant sensor 1 readings increase immediately following a prominent trough, reflecting the biomechanical fact that heel strike initiates stance. For all other sensors, early readings were discarded until their values exceeded a sensor-specific activation threshold δ that accounts for MEMS sensor noise (threshold determination provided in the Supplementary Information). The end of a stance phase was identified based on the toe sensor (sensor 8). Once its pressure decreased by 50% from its stance-phase peak, the toe sensor value and all other sensor outputs were set to zero, marking the end of the stance cycle. The toe-off compensation method was developed through analysis of a population dataset [25], with details provided in the Supplementary Information. All trials across the different scenarios were finally matched in length (i.e., number of time samples). The shortest trial was identified, and all other trials were down sampled to this length. For each scenario, an average trial was generated by computing the mean time-aligned sensor signal across all trials for each sensor.

3 | Results

3.1 | Optimal Sensor Placement

For this study, the test user was a 27-year-old, healthy individual. After splitting the foot area into the four zones, mean peak pressures (26 trials) of 307, 645, 61, and 518 kPa were identified for the toe, forefoot, midfoot, and heel, respectively. The loading coefficient matrix of the first principal component was used, capturing 51.6% of the total variance of the user's dataset.

In this study, eight sensors in total were considered to balance readout speed and overall sensor performance, whilst the foot was arbitrarily segmented into four regions: heel, midfoot, forefoot, and toes. The optimal placement resulted in three sensors in the heel region, four in the forefoot and one in the toe area. Comparing the CoP tracking performance of the optimally placed sensor subset to the full pressure plate output, mean errors of 2.52 ± 2.18 mm in the mediolateral (ML) direction and 6.61 ± 6.48 mm in the anteroposterior (AP) direction were observed (Figure S2).

3.2 | The Sole Cooptimization Pipeline

The goal of the cooptimization process is to select a lattice geometry that ensures mechanical support tailored to the user, while maximizing sensing performance (range, spatial resolution, and sensitivity) for each region of the sole. Thanks to the design of the sole, its mechanical and sensing properties are tightly coupled: a stiffer lattice will produce less pressure change in the associated chambers, leading to a less sensitive sensor; a larger unit cell increases the base area of the pyramid chamber, reducing the spatial resolution of the final sensor.

Starting from the user dataset, captured using a standard pressure plate in a lab environment, the steps for the cooptimization process are the following

1. Segment the foot in four regions (heel, mid-foot, front-foot and toe area) and identify the regional peak pressure values P_{reg}.
2. Identify optimal sensor locations for each region, considering foot pressure distribution and total number of sensors desired.
3. Assign the optimal lattice geometry based on a score metric combining mechanical and sensing needs.
4. Manufacture the final design according to the identified optimal lattice parameters.

3.3 | FEA Analyses and Lattice Configuration

Figure 2a shows the FEA results. The resulting unit cells can withstand maximum foot pressures of up to 5 MPa, higher than the ones measured in lab tests [25], and equivalent stiffness K ranging from 4.98 to 1400 Nmm^{-1}. As expected, a lower λ, denser lattice, is associated with unit cells capable of withstanding higher loads (Figure 2a), while, for the same λ, a decrease in L produces softer lattices. The resulting maximum predicted air-pressure change $\Delta Q_{\max}$ for each unit cell increases with larger λ, largely independent of L (centre chart of Figure 2a): chambers with the same relative density λ display equivalent compression levels. The chamber area A_{c}, instead, grows as expected with increasing strut length L at fixed density λ and with increasing λ at fixed L (Figure 2a).

Figure 2b highlights the complex, interdependent relationships between the three sole properties just analyzed and sensor-level performance in terms of sensing range, spatial resolution and sensitivity. Two cases, constant λ and constant L, are considered separately to isolate positive and negative correlations between variables. Some of these are straightforward: the chamber area can be considered a direct proxy for spatial resolution, in the same way as the stiffness directly maps to the sensitivity—as the first one in each pair increases, the second one decreases (blue lines in both charts). Other relationships change sign (connecting line has different colours in the charts) based on how the change in one of the three variables of the top semi-circle is obtained. For example, an increase in stiffness at fixed λ produces a lattice that has a larger chamber area, with negative effects on the final spatial resolution of the sensor. The opposite is true when increasing stiffness while keeping L fixed, as this means moving to thicker struts and a lower chamber area. Any metric used for optimizing the lattice geometry needs to integrate these interdependencies and trade-offs among variables for the process to be successful, resulting in a cooptimization process which is at the core of the embodied intelligence approach to robot/device body morphology design.

In our case, rather than employing a full optimization framework, a simple and interpretable scoring function (Equation (7)) is adopted as a lattice selection strategy to demonstrate the effectiveness of the proposed pipeline. The scoring function was defined aiming to maximize the internal air-pressure change $\Delta Q_{\max}$ (maximize sensitivity) whilst minimizing cavity side length C (maximize spatial resolution) for a lattice able to withstand foot regional peak pressures P_{reg} associated to a specific user.

$$\mathrm{score}(\lambda, L) = \frac{f_{\mathrm{minmax}}\left(\frac{P_{\mathrm{reg}}}{P_{\max}} \Delta Q_{\max}\right)}{f_{\mathrm{minmax}}(C)} \tag{7}$$

Figure 2c displays the lattice selection result for a device meant for our test user. For each zone separately, lattices with a maximum load-bearing pressure $P_{\max}$ lower than the user's peak pressure P_{reg} were discarded. The same was done for unit cells with a cavity side-length $L - D$ lower than 5 mm and greater than 15 mm, to ensure pneumatic chambers large enough for the electronic pressure sensors whilst avoiding them becoming so large as to merge together adjacent optimal sensor locations. Within the scoring function, the numerator is a min–max normalized product of the ratio $P_{\mathrm{reg}}/P_{\max}$, which reflects how close the maximum operating pressure is to the lattice's load-bearing limit, and $\Delta Q_{\max}$, the predicted maximum air pressure response, representing the maximum air pressure variation. The denominator corresponds to the min–max normalized cavity side length C, which serves as a direct proxy for sensor spatial resolution. The score metric was then applied to the resulting search-space (Figure 2c, colored area in the charts), and the highest-scoring lattice was then selected (pink dot in each chart). Such a scoring function drives the selection toward lattice configurations with larger λ and smaller L within the feasible design space (Figure 2c), and the reasons can be understood through the sensing-mechnical relationship illustrated in Figure 2b. A smaller L leads to small chamber area, thereby improving spatial resolution, while a larger λ is associated with lower lattice stiffness and increased pressure sensitivity. Sensor cavities were then designed and placed in the optimal locations highlighted by the pink squares in the figure. For the midfoot region, where no sensor is placed, sensing performance is not optimized; instead, the highest relative density λ is chosen to maximize flexibility, and the strut length L is kept similar to the other regions.

To demonstrate the capability of the lattice selection process to generate diverse and user-centric lattice configurations, three use cases with different constraints based on Equation (7) are presented (Table S1).

To directly demonstrate the validity of the cooptimization pipeline proposed so far, two sensorised lattice samples, one from the heel section and one from the toe region, were compared to showcase the effect of optimal lattice selection on sensing performance (Figure S3). The optimal heel-region lattice, which must sustain 68.7% higher peak pressures, has a stiffness $K = 14.84$ Nmm^{-1}, 39.3% higher than the toe-region lattice at 10.65 Nmm^{-1}, whereas the two maintain similar spatial resolution (L differs by only 0.5 mm). The toe sensor unit (lattice and air-chamber) demonstrated the highest linearized sensitivity ($R^2 = 0.973$, RMSE = 5.71%), 6.2% higher than that of the heel unit tested over its full range ($R^2 = 0.987$, RMSE = 4.23%), with the latter exhibiting 60.6% higher sensor range. Furthermore, selecting a uniform stiffness sole would lead to a 65.8% drop in linearized sensitivity in the toe region ($R^2 = 0.976$, RMSE = 5.57%). Besides aligning with the analysis in Figure 2b, these results prove the potential of our embodied intelligence-inspired codesign pipeline to directly lead to better quality data straight out of the wearable device, prior to any postprocessing.

3.4 | Smart Shoe Characterization and Validation in Controlled Setting

Figure 3a reports the results for each sensor in terms of repeatability and hysteresis, which ranged from 0.7% to 1.6% of full scale and from 22% to 35.4% of full scale respectively. The higher hysteresis is linked to the materials used, which displayed similar marked viscoelastic behavior during characterization.

Figure 3b presents a cross-instrument comparison. Plantar pressures recorded during fast, flat walking with the smart shoe are compared against the precollected user-specific dataset obtained with the user walking barefoot on a Novel Emed-n50 pressure plate. For the shoe, plantar pressure was converted from air chamber pressures (details in Supplementary Information). In the trial, most shoe sensors presented higher peak plantar pressure values compared to the pressure plate, aligning with the results of [41] which reported that in-shoe measurements generally exceed those from a pressure plate, with maximum differences up to +206.3%. An interesting insight comes from comparing sensors 1 and 2 on the two devices. In the case of the pressure plate, sensor 2 has a much higher reading than sensor 1. The combination of barefoot walking together with the rigid nature of the pressure plate leads the heel strike to be more localized with a sharp peak around sensor 2. In contrast, the softer shoe conforms better to the foot, leading to a more pronounced rolling contact from the back to the front of the heel, as demonstrated by the peak in sensor 1 preceding that of sensor 2. Despite these differences, the average CoP trajectories derived from the plantar pressure measurements (shown on the left of the charts, together with their variability) align closely (Supplementary Materials and Methods: CoP trajectory alignment and variability computation). The lower CoP variability observed for the shoe is likely linked to the conformability of the sole and a possible targeting effect by the user trying to land in the same sensing region on the plate [41]. Despite this transversal variability of the CoP trajectories, the longitudinal point density along the CoP trajectory follows similar trends, with high density in the heel and forefoot area and low density through the midfoot region, meaning that

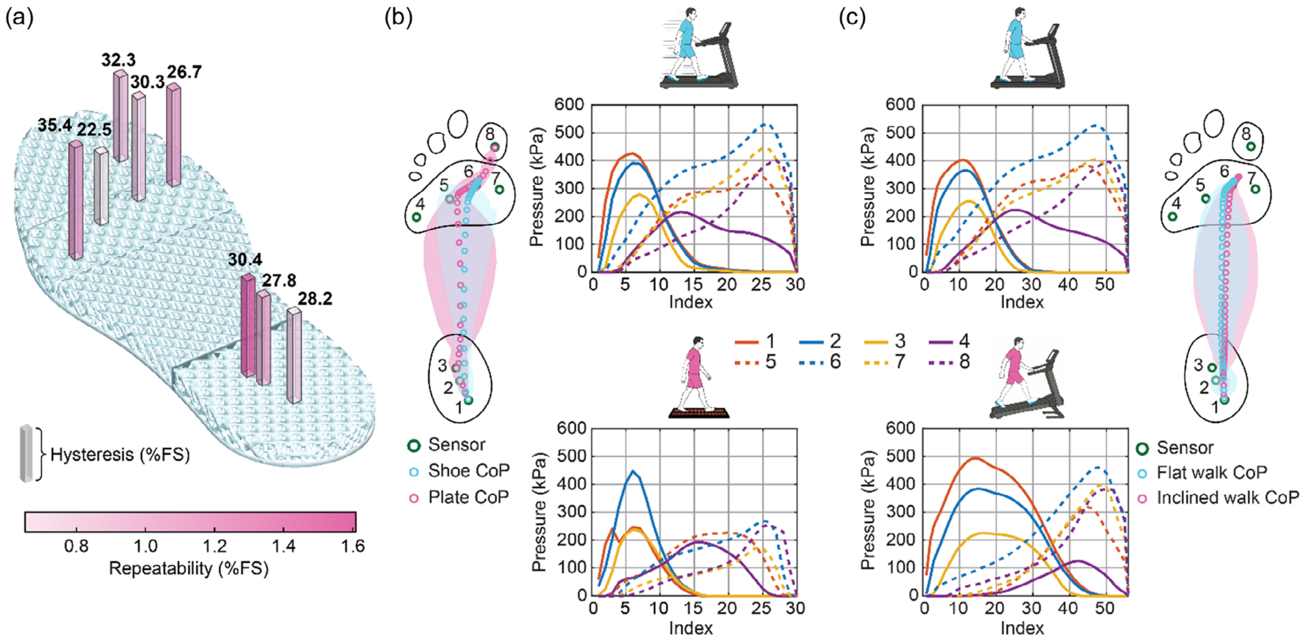

FIGURE 3 | Smart shoe characterization and validation in controlled setting. (a) Device calibration results showing full-scale normalized hysteresis and repeatability for all sensors (3 loading-unloading cycles per sensor) (Figure S4). (b) Plantar pressure data recorded during fast flat walking at 5 km/h with the shoe (light blue) on a treadmill compared against a user-specific dataset collected using an Emed-n50 pressure plate (Novel GmbH, Germany) (pink). For both datasets, the averaged sensor readings, mean CoP trajectory, and CoP trajectory variability (15 steps for the shoe and 26 steps for the plate) are presented. The accompanying charts display individual sensor outputs to highlight gait-phase lengths. (c) Plantar pressure data for slow walking (4 km/h) on flat treadmill compared to walking with an 8.5° inclination. For both datasets, the averaged sensor readings, mean CoP trajectory, and CoP trajectory variability (light blue and pink shaded areas) are presented. The charts highlight a lengthened heel phase in the inclined walking compared to the flat walking case, a known result in the literature.

comparable ratios of gait phases are observed between walking with and without the shoe.

Figure 3c shows the comparison between slow (4 km/h) flat walking and slow inclined walking (8.5°). The average peak pressures recorded are generally similar across sensors except for sensor 1: in the inclined condition its peak reaches 500 kPa compared with 400 kPa in the flat walk. More importantly, during inclined walking, the heel sensors exhibit a slower pressure decline and a higher pressure–time integral while the forefoot sensors show a lower pressure–time integral. These trends, aligned with the results reported by [42] for similar testing conditions, lead to a shift in the CoP trajectories and denser point-clouds in the heel region for the inclined walking. Apart from this difference, the average CoP trajectories largely coincide, and variability remains similar between conditions—mean standard deviation in the medial–lateral (ML) direction: 2.56 mm versus 1.80 mm, and in the anterior–posterior (AP) direction: 8.03 mm versus 10.85 mm for flat and inclined walking, respectively. The results for fast flat and inclined walking are presented in Figure S5 and display similar trends.

Moreover, comparing walking with the device on the flat treadmill under fast (5 km/h) and slow (4 km/h) walking conditions (Figure 3b,c), the average pressure profiles for each sensor, including their peak pressures and overall trends, remain broadly consistent across gait speeds. The corresponding CoP trajectories also largely align between the two conditions.

A comparative study (Table S2) was conducted between the proposed lattice configurations and those reported in prior work [43] using the flat fast walk data (Figure 3b). The differences between the two studies can be attributed to variations in materials and lattice topology, with the prior study [39] employing closed-cell lattice structures that exhibit higher stiffness, resulting in higher peak stress and lower displacement compared to the present work.

3.5 | Validation in Target Application

A final validation was performed outside the laboratory under more varied locomotion, surface, and friction conditions than those encountered during treadmill experiments to demonstrate the potential of the shoe as a real-time monitoring device in everyday activities and environments where a pressure plate cannot be used. These scenarios included walking outdoors on grass and ascending and descending stairs (Video S2). The results are presented in Figure 4, where, for each scenario, the mean peak pressure, the CoP trajectories and their progression, and an example trial are shown.

Figure 4a shows the results of walking on grass. Compared with the laboratory-based flat walking experiments (Figure 3), the heel sensors record similar mean peak pressures and a larger pressure-time integral. On the contrary, the forefoot sensors show much lower mean peak pressures, indicating a reduced forefoot push-off force, expected because of the softer interface provided by the grass. This results in CoP trajectories originating at the heel and terminating shortly after entering the forefoot region.

When ascending stairs (Figure 4b), the forefoot sensors record significantly higher mean peak pressures than the heel sensors, consistent with the greater mechanical loading on the forefoot during push-off compared to normal walking. The CoP trajectories display greater variability at the start, with some originating at the heel and others at the forefoot or toes. This variability mirrors changes, also recorded on video, in which part of the foot first contacts the stair. In contrast, all trajectories consistently terminate in the forefoot region, reflecting its role in generating push-off at the end of a step. In the example trial, contact is first registered at the forefoot and toes (index 1–5). The weight is then shifted toward the heel (12 to 30), before finally reaching the push-off phase (index 70), when forefoot and toe sensors register their peaks.

Contrary to the previous case, when descending stairs, mean peak pressure values are more evenly distributed between the heel and forefoot regions (Figure 4c). All CoP trajectories start in the midfoot or forefoot, reflecting typical stair descent gaits, where contact with the downward step is first made with the front of the foot, or with the entire foot simultaneously, with no discernible heel strike. The trajectories move between the heel and forefoot regions and ultimately terminate in the forefoot as push-off occurs before the foot leaves the step. This trends, which result in inversions (posterior and then anterior paths) of the CoP trajectories, are well-illustrated by the example trial chart. At the start of the step (index 1–5), the forefoot sensors register non-zero pressure while the heel sensors remain inactive. Heel sensors become active only after index 10 as the midfoot and heel support the body's weight and downward inertia, and their readings remain lower than those of some forefoot sensors. At index 62, sensor 7 records a pronounced peak, indicating the moment of forefoot push-off.

4 | Discussion

This work introduced an embodied intelligence-inspired design pipeline that jointly optimizes the mechanical and sensing properties of a smart sole to meet personalized requirements. To demonstrate the pipeline's capability, a device was fabricated for a target user using a small, precollected plantar pressure dataset to define the individual's design constraints. The experiments demonstrated how the resulting device could capture CoP trajectory in line with state-of-the-art platform systems and do so in real-time and in a variety of settings, within and outside the laboratory, with just eight sensors, unlike most other in-shoe plantar pressure devices, which are designed exclusively to maximize sensing spatial resolution. In addition, this work demonstrates a practical manufacturing and integration strategy that enables airtight pneumatic chambers and flexible PCB sensing modules to be embedded within a 3D-printed lattice structure. Besides improving data quality and reducing data throughput, combining sensing and personalized requirements in a cooptimization process allows the creation of wearables that function as measurement devices while preserving desired mechanical properties for the target user. Targeted regional stiffness and peak-pressure reduction are widely regarded as essential strategies for prevention and treatment of diabetic foot ulcers [44–46], which can lead to

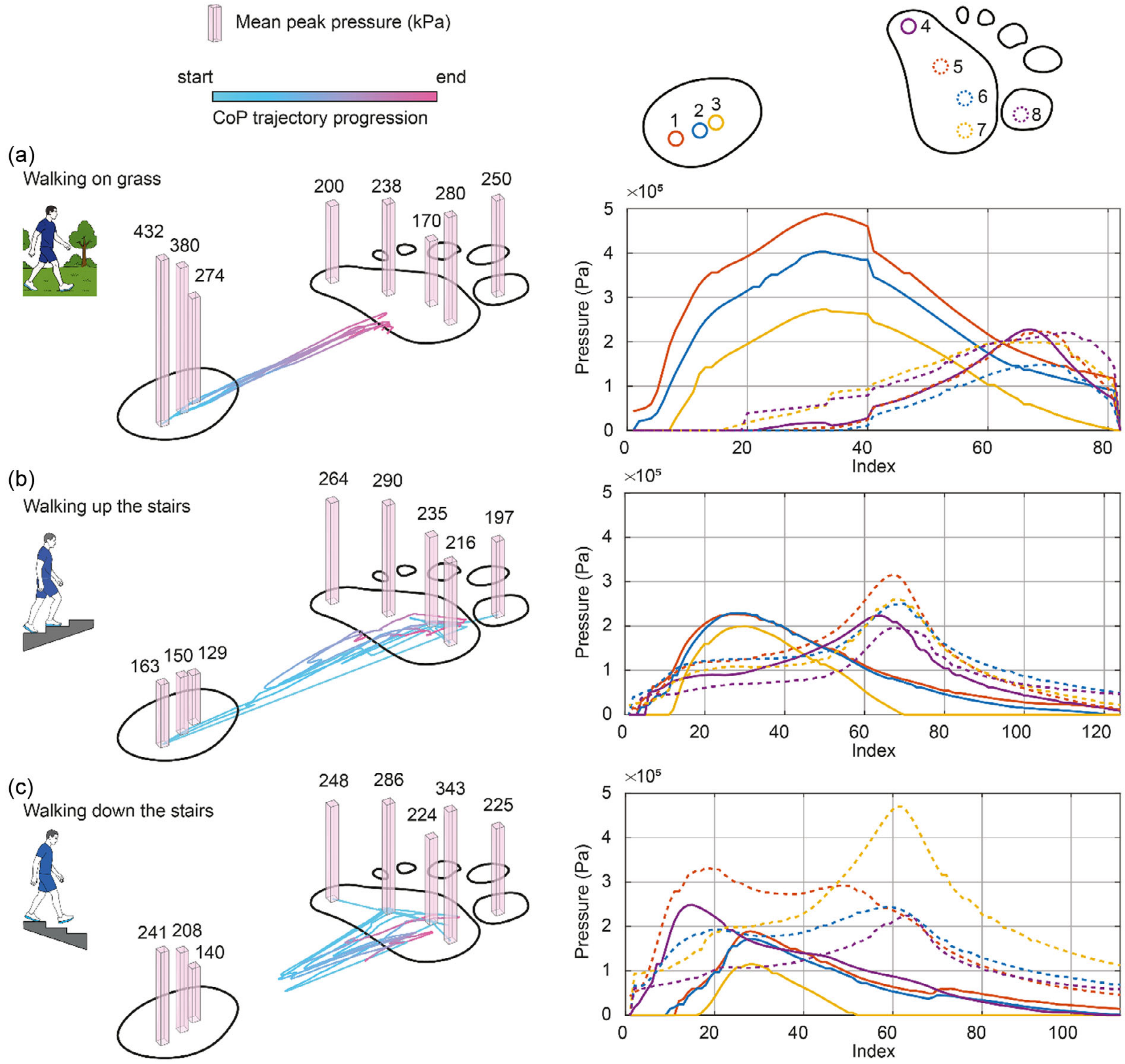

FIGURE 4 | Out-of-laboratory gait experiments. For each scenario, the average peak pressure (5 trials), CoP trajectory progression and an example trial are shown. (a) When walking on grass, heel peak pressures are comparable to those during treadmill walking, whereas forefoot peak pressures are markedly lower, reflecting the reduced push-off force on the compliant surface. (b) For stair ascent, the low mean peak pressures at the heel, together with the widely varying starting points of the CoP trajectories, reflect inconsistent initial foot contact. In contrast, forefoot push-off is evident, as shown by the higher mean peak pressures in the forefoot and the consistent termination of all CoP trajectories near the forefoot region. (c) For stair descent, all CoP trajectories originate in the midfoot or forefoot, indicating that initial contact occurs either with the forefoot alone or with the whole foot placed simultaneously, with no heel strike observed. The trajectories consistently terminate in the forefoot region, reflecting the push-off phase at the end of each step and displaying interesting inversions in the CoP trajectories.

lower-extremity amputation in up to 20% of cases [47]. Furthermore, effective real-time CoP tracking enables activity recognition and extraction of features that are associated with balance and fall risk in elderly [48] and poststroke patients [49].

A key limitation in the development of tailored wearable devices is linked to the availability of 3D printing materials with appropriate mechanical properties. 3D printing polymers tend to display pronounced hysteretic behavior and mechanical properties of functionalized materials are usually not the priority in their development. In this study, a simplified FEM model with empirical compensation was adopted, despite the rate-dependent behavior of the elastomeric material. The FEM results were therefore used primarily to compare and rank lattice configurations within the design space, rather than to provide exact quantitative predictions of the final device response. Although the Instron Universal Testing Machine can reach compression speeds comparable to those during gait, its relatively long acceleration phase and short compression distance result in a lower effective loading rate, making it less representative of the rapid compression experienced in real walking conditions. Furthermore, while the FEM model was validated and shown to achieve acceptable agreement with experimental results, two directions for improvement can be identified: (1) refining the FEM formulation to further enhance modeling accuracy and (2) incorporating more advanced material models to capture viscoelastic behavior. Relying, as in this study, on a combination of pneumatic sensing and lattice structures provides good adaptability to a wide range of materials and 3D printing techniques, even though the core principle can also be extended to other structures and sensing modalities. In this study, focus was mostly on sensing, but the optimization framework and scoring function can be extended to include more nuanced mechanical requirements, such as regional or anisotropic stiffness profiles and damping coefficients, to enable broader personalization. While the overall geometry was kept simple, maintaining a constant thickness throughout the sole, more complex geometries can be considered for improved comfort and arch support, representing further inputs for the cooptimization process.

In the future, we see smart wearables as key in improving our health through continuous biomarker monitoring. Our proposed embodied intelligence-inspired approach represents a step in this direction, allowing devices to carry as little sensing as possible while improving data quality, reducing cost and energy consumption, and respecting key mechanical performance requirements. Future effort will also be spent in improving the framework by looking not just at optimized sensor placement but overall sensor morphology to improve data quality further. The inclusion of AI algorithms on edge devices together with sensor fusion enabled by the reduction of the overall data throughput for real-time patient monitoring will serve as a final validation benchmark for our approach.

Author Contributions

F.Z., and M.P. contributed to formal analysis, investigation, software, validation, visualization; F.Z., M.P. and P.M. contributed to methodology; F.Z. contributed to data curation; M.P., A.Z., and P.M. contributed to conceptualization; M.P. and P.M. contributed to project administration; P.M. contributed to funding acquisition and resources; A.Z. and P.M. contributed to supervision; F.Z., M.P. contributed to writing – original draft; F.Z., M.P., A.Z., and P.M. contributed to writing – review and editing.

Acknowledgments

This work was supported by the Engineering and Physical Sciences Research Council (EPSRC) through Grant EP/V000748/1. The authors acknowledge the help of Igor Dyson for helping with the material characterisation experiments and of Leone Costi for the FEA analyses setup.

Funding

This study was supported by Engineering and Physical Sciences Research Council (EP/V000748).

Conflicts of Interest

The authors declare no conflicts of interest.

Data Availability Statement

All data and code needed for the replicationof the study will be made available through the University of Oxford Research Data Archive *ORA*.

References

1. M. Flores, G. Glusman, K. Brogaard, N. D. Price, and L. Hood, “P4 Medicine: How Systems Medicine Will Transform the Healthcare Sector and Society,” *Personalized Medicine* 10 (2013): 565–576.

2. M. Braun, “How Predictive Medicine Leads to Solidarity Gaps in Health,” *npj Digital Medicine* 8 (2025): 111.

3. R. Pfeifer, M. Lungarella, and F. Iida, Self-Organization, Embodiment, and Biologically Inspired Robotics.

4. H. Hauser, A. J. Ijspeert, R. M. Füchslin, R. Pfeifer, and W. Maass, “Towards a Theoretical Foundation for Morphological Computation with Compliant Bodies,” *Biological Cybernetics* 105 (2011): 355–370.

5. C. Laschi, B. Mazzolai, and M. Cianchetti, “Soft Robotics: Technologies and Systems Pushing the Boundaries of Robot Abilities,” *Science Robotics* 1 (2016): eaah3690.

6. L. He, N. Herzig, T. Nanayakkara, and P. Maiolino, “3D-Printed Soft Sensors for Adaptive Sensing with Online and Offline Tunable Stiffness,” *Soft Robotics* 9 (2022): 1062–1073.

7. M. A. McEvoy and N. Correll, “Materials that Couple Sensing, Actuation, Computation, and Communication,” *Science* 347 (2015): 1261689.

8. F. Corucci, N. Cheney, F. Giorgio-Serchi, J. Bongard, and C. Laschi, “Evolving Soft Locomotion in Aquatic and Terrestrial Environments: Effects of Material Properties and Environmental Transitions,” *Soft Robotics* 5 (2018): 475–495.

9. G. Mengaldo, F. Renda, S. L. Brunton, et al., “A Concise Guide to Modelling the Physics of Embodied Intelligence in Soft Robotics,” *Nature Reviews Physics* 4 (2022): 595–610.

10. M. Lalegani Dezaki, R. Sales, A. Zolfagharian, H. Yazdani Nezhad, and M. Bodaghi, “Soft Pneumatic Actuators with Integrated Resistive Sensors Enabled by Multi-Material 3D Printing,” *International Journal of Advanced Manufacturing Technology* 128 (2023): 4207–4221.

11. Q. Wang, “A Wireless, Self-Powered Smart Insole for Gait Monitoring and Recognition via Nonlinear Synergistic Pressure Sensing,” *Science Advances* (2025).

12. J. Tao, M. Dong, L. Li, et al., “Real-Time Pressure Mapping Smart Insole System Based on a Controllable Vertical Pore Dielectric Layer,” *Microsystems and Nanoengineering* 6 (2020): 62.

13. Q. Zhang, Y. L. Wang, Y. Xia, X. Wu, T. V. Kirk, and X. D. Chen, “A Low-Cost and Highly Integrated Sensing Insole for Plantar Pressure Measurement,” *Sensing and Bio-Sensing Research* 26 (2019): 100298.

14. M. Ntagios and R. Dahiya, “3D Printed Soft and Flexible Insole With Intrinsic Pressure Sensing Capability,” *IEEE Sensors Journal* 23 (2023): 23995–24003.

15. A. H. Abdul Razak, A. Zayegh, R. K. Begg, and Y. Wahab, “Foot Plantar Pressure Measurement System: A Review,” *Sensors* 12 (2012): 9884–9912.

16. X. Xian, Z. Zhou, G. Huang, J. Nong, B. Liu, and L. Xie, “Optimal Sensor Placement for Estimation of Center of Plantar Pressure Based on the Improved Genetic Algorithms,” *IEEE Sensors Journal* 21 (2021): 28077–28086.

17. C.-W. Lin, S.-J. Ruan, W.-C. Hsu, Y.-W. Tu, and S.-L. Han, “Optimizing the Sensor Placement for Foot Plantar Center of Pressure without Prior Knowledge Using Deep Reinforcement Learning,” *Sensors* 20 (2020): 5588.

18. M. R. Binelli, et al., “Digital Manufacturing of Personalised Footwear with Embedded Sensors,” *Scientific Reports* 13 (1962): 2023.

19. J. Lee, J. Lee, Y. J. Lee, et al., “Flexible Smart Insole and Plantar Pressure Monitoring Using Screen-Printed Nanomaterials and Piezoresistive Sensors,” *ACS Applied Materials and Interfaces* 17 (2025): 47153–47161.

20. A.-R. A. Laaraibi, G. Jodin, D. Hoareau, N. Bideau, and F. Razan, “Flexible Dynamic Pressure Sensor for Insole Based on Inverse Viscoelastic Model,” *IEEE Sensors Journal* 23 (2023): 7634–7643.

21. X. Hu, Q. Duan, J. Tang, et al., “A Low-Cost Instrumented Shoe System for Gait Phase Detection Based on Foot Plantar Pressure Data,” *IEEE Journal of Translational Engineering in Health and Medicine* 12 (2024): 84–96.

22. S. Mahmud, A. Khandakar, M. E. H. Chowdhury, et al., “Fiber Bragg Gratings Based Smart Insole to Measure Plantar Pressure and Temperature,” *Sensors and Actuators A: Physical* 350 (2023): 114092.

23. X. Li, X. Liu, W. Zeng, et al., “Carbon Fiber-Based Smart Plantar Pressure Mapping Insole System for Remote Gait Analysis and Motion Identification,” *Advanced Materials Technologies* 8 (2023): 2300095.

24. F. Zhong, L. He, A. Zavatsky, and P. Maiolino, “A Sensor Placement Benchmarking Method With Principal Component Analysis,” *IEEE Transactions on Instrumentation and Measurement* 72 (2023): 1–9.

25. B. G. Booth, N. L. W. Keijsers, T. Huysmans, and J. Sijbers, CAD WALK Healthy Controls Dataset.

26. B. Ren and J. Liu, “Design of a Plantar Pressure Insole Measuring System Based on Modular Photoelectric Pressure Sensor Unit,” *Sensors* 21 (2021): 3780.

27. Y. Sun, Q. Zhou, W. Niu, et al., “3D Printed Sports Shoe Midsoles: Enhancing Comfort and Performance through Finite Element Analysis of Negative Poisson’s Ratio Structures,” *Materials and Design* 245 (2024): 113292.

28. L.-P. Kang and T.-S. Gong, “Design of 3D Printed Pressure-Reducing Insoles Based on Changes in Parameters of Lattice Structure,” *Advances in Mechanical Engineering* 15 (2023): 16878132231216609.

29. R. Sakura, et al., “LattiSense: A. 3D-Printable Resistive Deformation Sensor with Lattice Structures,” in Proceedings of the 8th ACM Symposium on Computational Fabrication (ACM, 2023), 1–4, https://doi.org/10.1145/3623263.3623361.

30. C. Carradero Santiago, C. Randall-Posey, A.-A. Popa, et al., “3D Printed Elastomeric Lattices With Embedded Deformation Sensing,” *IEEE Access* 8 (2020): 41394–41402.

31. J.-L. Chen, Y.-N. Dai, N. S. Grimaldi, et al., “Plantar Pressure-Based Insole Gait Monitoring Techniques for Diseases Monitoring and Analysis: A Review,” *Advanced Materials Technologies* 7 (2022): 2100566.

32. K. Kong and M. Tomizuka, “A Gait Monitoring System Based on Air Pressure Sensors Embedded in a Shoe,” *IEEE/ASME Transactions on Mechatronics* 14 (2009): 358–370.

33. D. A. Jacobs and D. P. Ferris, “Estimation of Ground Reaction Forces and Ankle Moment with Multiple, Low-Cost Sensors,” *Journal of NeuroEngineering and Rehabilitation* 12 (2015): 90.

34. K. Kim, S. Shin, and K. Kong, “An Air-Filled Pad With Elastomeric Pillar Array Designed for a Force-Sensing Insole,” *IEEE Sensors Journal* 18 (2018): 3968–3976.

35. A. Zolfagharian, M. R. Khosravani, H. Duong Vu, M. K. Nguyen, A. Z. Kouzani, and M. Bodaghi, “AI-Based Soft Module for Safe Human–Robot Interaction towards 4D Printing,” *Polymers* 14 (2022): 3302.

36. Y. Yao, L. He, and P. Maiolino, “A Simulation-Based Toolbox to Expedite the Digital Design of Bellow Soft Pneumatic Actuators,” in 2022 IEEE 5th International Conference on Soft Robotics (RoboSoft) (2022), 29–34, https://doi.org/10.1109/RoboSoft54090.2022.9762153.

37. V. S. Deshpande, N. A. Fleck, and M. F. Ashby, “Effective Properties of the Octet-Truss Lattice Material,” *Journal of the Mechanics and Physics of Solids* 49 (2001): 1747–1769.

38. K. Lehner, A. Kalteis, and Z. Major, “Modelling and Simulation of Lattice Structures Using Various Material Models for Polymeric Materials,” *Acta Polytechnica CTU Proceedings* 18 (2018): 48.

39. A. Hössinger-Kalteis, “Design Method for Individualised 3D Printed Lattice Shoe Midsoles,” *Proceedings of the Institution of Mechanical Engineers, Part L: Journal of Materials: Design and Applications* 239 (2025): 1422–1432.

40. S. C. Fay, Optimizing Shoe Midsoles for Running Performance.

41. C. M. Amaro, “Comparative Analysis of Pressure Platform and Insole Devices for Plantar Pressure Assessment,” *Applied Sciences* 15 (2025): 7575.

42. S. C. Wearing, S. R. Urry, and J. E. Smeathers, The Effect of Visual Targeting on Ground Reaction Force and Temporospatial Parameters of Gait.

43. A. Zolfagharian, M. Lakhi, S. Ranjbar, and M. Bodaghi, “Custom Shoe Sole Design and Modeling Toward 3D Printing,” *International Journal of Bioprinting* 7 (2021): 396.

44. S. Koo, M. S. Park, C. Y. Chung, et al., “Effects of Walking Speed and Slope on Pedobarographic Findings in Young Healthy Adults,” *PLOS ONE* 14 (2019): e0220073.

45. S. Ahmed, A. Barwick, P. Butterworth, and S. Nancarrow, “Footwear and Insole Design Features that Reduce Neuropathic Plantar Forefoot Ulcer Risk in People with Diabetes: A Systematic Literature Review,” *Journal of Foot and Ankle Research* 13, no. 1 (2020).

46. R. Collings, J. Freeman, J. M. Latour, and J. Paton, “Footwear and Insole Design Features for Offloading the Diabetic at Risk Foot—A Systematic Review and Meta-Analyses. Endocrinology,” *Diabetes and Metabolism* 4 (2021): e00132.

47. M. Nouman, T. Dissaneewate, D. Y. R. Chong, and S. Chatpun, “Effects of Custom-Made Insole Materials on Frictional Stress and Contact Pressure in Diabetic Foot with Neuropathy: Results from a Finite Element Analysis,” *Applied Sciences* 11 (2021): 3412.

48. K. McDermott, M. Fang, A. J. M. Boulton, E. Selvin, and C. W. Hicks, “Etiology, Epidemiology, and Disparities in the Burden of Diabetic Foot Ulcers,” *Diabetes Care* 46 (2023): 209–221.

49. F. Quijoux, A. Vienne-Jumeau, F. Bertin-Hugault, et al., “Center of Pressure Characteristics from Quiet Standing Measures to Predict the Risk of Falling in Older Adults: A Protocol for a Systematic Review and Meta-Analysis,” *Systematic Reviews* 8 (2019): 232.

Supporting Information

Additional supporting information can be found online in the Supporting Information section.